Nonlinear dynamics of a horizontal rotor with asymmetric magnetic supports

International Journal of Non–Linear Mechanics 165 (2024) 104764

Contents lists available at ScienceDirect

International Journal of Non-Linear Mechanics

journal homepage: www.elsevier.com/locate/nlm

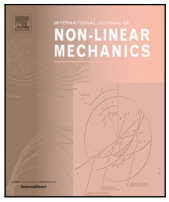

Nonlinear dynamics of a horizontal rotor with asymmetric magnetic supports

Salvatore Paolo Cavallaro, Simone Venturini *, Elvio Bonisoli

Department of Mechanical and Aerospace Engineering, Politecnico di Torino, Corso Duca degli Abruzzi, 24, 10129, Torino, Italy

ARTICLE INFO

Keywords:
Rotordynamics
Magnetic levitation
Passive magnetic bearings
Time–frequency analysis

ABSTRACT

In this paper, a horizontal rotor with passive anisotropic asymmetric magnetic bearings nonlinear model is developed. The model is based on the experimental evidence of an educational demonstrator, a powerful benchmark which highlights features of rotordynamics systems. An experimental setup is developed using laser sensors to track the displacements of the rotor and tachometer to record the rotor angular speed. Several test campaigns are performed with different initial conditions to characterise the educational demonstrator. The first test campaign is oriented to identify the system structural properties, while the second one is focused on the nonlinearity identification. The rotor modelling is divided into three stages with progressive increase in complexity, starting from the overall linear structural behaviour to the nonlinear subharmonic resonance phenomenon. The model is developed with a generalised approach suitable for a wide range of operating conditions and rotor configurations. Progressively, the developed rotor models are compared to highlight their limitations and advantages. Finally, rotor trajectory analysis and time–frequency analysis are used in the numerical-to-experimental comparison.

1. Introduction

In the last 20 years there has been a growing interest in the study of the magnetic interaction. The magnetic interaction is successfully exploited in mechanical power transmission devices. The magnetic gears [1] provide an alternative to conventional gears and increase transmission efficiency [2].

The magnetic interaction is adopted for the realisation of Active Magnetic Bearings (AMB) and Passive Magnetic Bearings (PMB) to eliminate the contact friction losses of the rotating components. In AMBs the magnetic force is generated by feedback control of electromagnetic coils [3], while PMBs use permanent magnets which do not require any control [4].

AMBs are employed in industrial applications for turbomachinery and flywheels, and their use in nuclear and submarine environments is currently subject of scientific research. Additionally, the following problems concerning AMBs are investigated: high-speed applications, control of elastic rotors, touch-down dynamics, and their use as elements for the realisation of smart rotating machinery with features such as self-calibration, self-diagnostics, self-tuning and self-corrections [3].

On the other side, PMBs are not used in stand-alone configuration in industrial applications as much as AMBs, and they find use in hybrid solutions for rotating machines together with the latter [5,6]. PMBs are often used in combination with AMBs in flywheels for kinetic energy storage [7], to reduce the AMBs control energy consumption requirements. Recently, there has been a growing interest in kinetic energy storage, also in the automotive field [8–12]. The growing interest in studying typical dynamic problems of rotor industrial systems lets the researchers propose practical solutions as the ones described in [13–15].

In education, PMBs find wide usage in magnetic interaction demonstrators, such as:

- the Levitron®, a levitating vertical-axis magnetic spinning top, is stable within a precise operating range due to the gyroscopic effect [16].
- the levitation toy, a horizontal-axis magnetically supported structure which is stable due to the presence of a further constraint. It is possible to spin the toy as a spinning top, highlighting typical rotordynamics characteristics.

This study is focused on the levitation toy dynamics. The levitation toy is a significant benchmark for nonlinear rotor behaviour modelling due to the magnetic support asymmetry and anisotropy [17]. Since this demonstrator shows typical features of rotor systems, an experimental analysis on the horizontal magnetic spinning top is performed to propose a possible investigation and modelling methodology.

This study is organised in the following sections, proposing the analysis from an experimental perspective up to the modelling phase and successive model updating:

* Corresponding author.
E-mail address: simone.venturini@polito.it (S. Venturini).

https://doi.org/10.1016/j.ijnonlinmec.2024.104764
Received 16 May 2023; Received in revised form 6 February 2024; Accepted 23 May 2024
Available online 1 June 2024

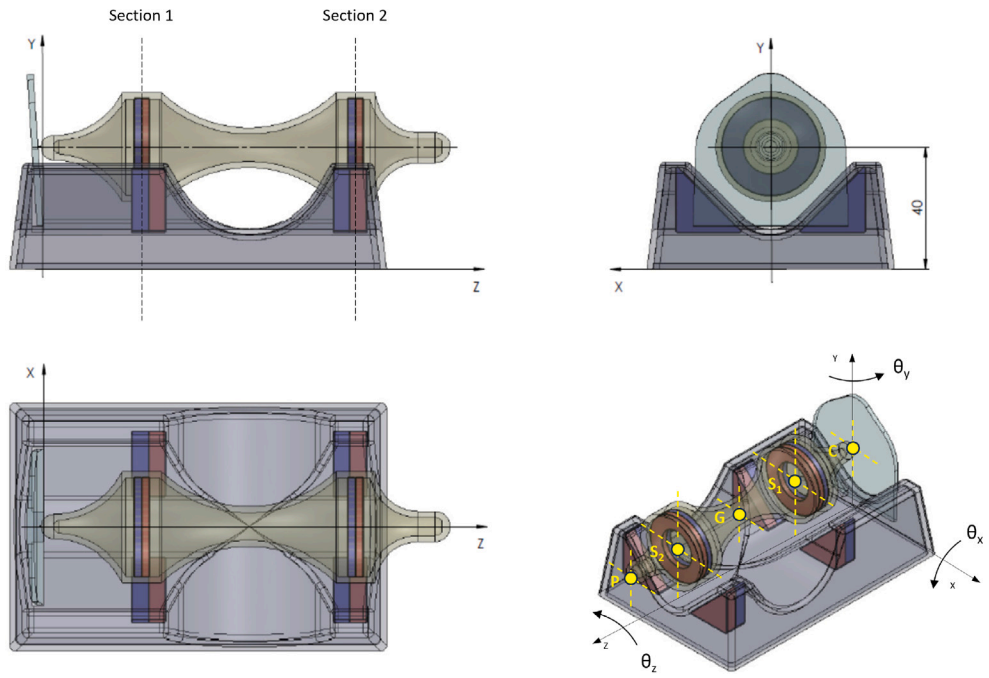

Fig. 1. SolidWorks model of horizontal magnetic rotor.

- Section 2 illustrates the demonstrator geometry and its material properties. Also, a critical review of the device, preliminary to the rotordynamics modelling, is performed.
- In Section 3, the experimental setup is described, and the experimental campaigns are performed. The acquisitions are discussed illustrating the main outcomes useful to develop the rotor models. Time–frequency analyses and time histories are investigated.
- In Section 4, the magnetic support modelling process is defined. Also, the generalised magnetic interaction maps and the analytical formulation are developed.
- In Section 5, the rotor models are developed. The models are compared with the experimental angular speed sweep down tests.
- Finally, in Section 6 the outcomes of the experimental and modelling activities are discussed, focusing also on future developments.

2. Device characteristics

The magnetic levitation toy under analysis in Fig. 1 is composed of two bodies under magnetic interaction:

- a fixed plastic base with prismatic triangular magnets placed inside.
- a floating axisymmetric plastic rotor, with annular disc magnets placed inside.

The magnets are placed in two axial regions, named sections, of the structure and together they compose the rotor magnetic supports. Fig. 1 highlights the rotor sections #1 and #2, which correspond to the middle planes of the floating magnets of the two respective supports. The interaction between the rotor and the base magnets makes the rotor levitate.

When the rotor is not rotating, one of the two rotor ends is always in contact with the base glass plate. In fact, Earnshaw theorem [18] demonstrated that a system subject to passive magnetic forces only does not have a stable static equilibrium. In this application, the levitation toy stable static equilibrium condition is guaranteed by the axial constraint at one rotor end. In fact, the floating and fixed magnet axial locations are designed to generate axial force pushing against the base glass plate. Fig. 1 shows in detail the floating and fixed magnets configuration allowing the rotor to reach a stable static equilibrium condition.

When the rotor is spun, it rotates with limited air drag losses, and reduced friction losses by the only base-rotor contact point. The stability of horizontal rotors has already been theoretically demonstrated by L.A. Romero [19] on a more generic non-axially constrained configurations. As can be seen in Fig. 1, the magnets inside the base are only under and on the sides of the floating rotor. Therefore, the base-rotor magnetic interaction is horizontally symmetric and vertically asymmetric.

In the experimental activity, five points of the rotor axis are identified and highlighted by yellow markers in Fig. 1:

- rotor magnetic support section centres S_1 and S_2 with rotor horizontal and vertical displacements x_1, y_1, x_2, and y_2;
- rotor barycentre G with horizontal and vertical displacements x_g, y_g;
- rotor contact point C with horizontal and vertical displacements x_c, y_c;
- rotor free end P with horizontal and vertical displacements x_p, y_p.

The details about the levitation toy geometry used in Section 5, are shown in Table 1.

Since the investigated device does not include any datasheet, common low performance ferrite magnet residual magnetic induction B_r is considered. In Table 1, the mean value between Y10T ($B_r = 0.200 \div 0.235$ T) and Y22H ($B_r = 0.310 \div 0.360$ T) is chosen.

3. Experimental activity

The experimental setup shown in Fig. 2 is developed to perform experimental activity.

The experimental setup is composed of a gantry structure which supports Laser sensors around the levitation device. The levitation device is positioned at the centre of the gantry structure, and the base is secured by adhesive material to prevent it from moving during the experimental activity.

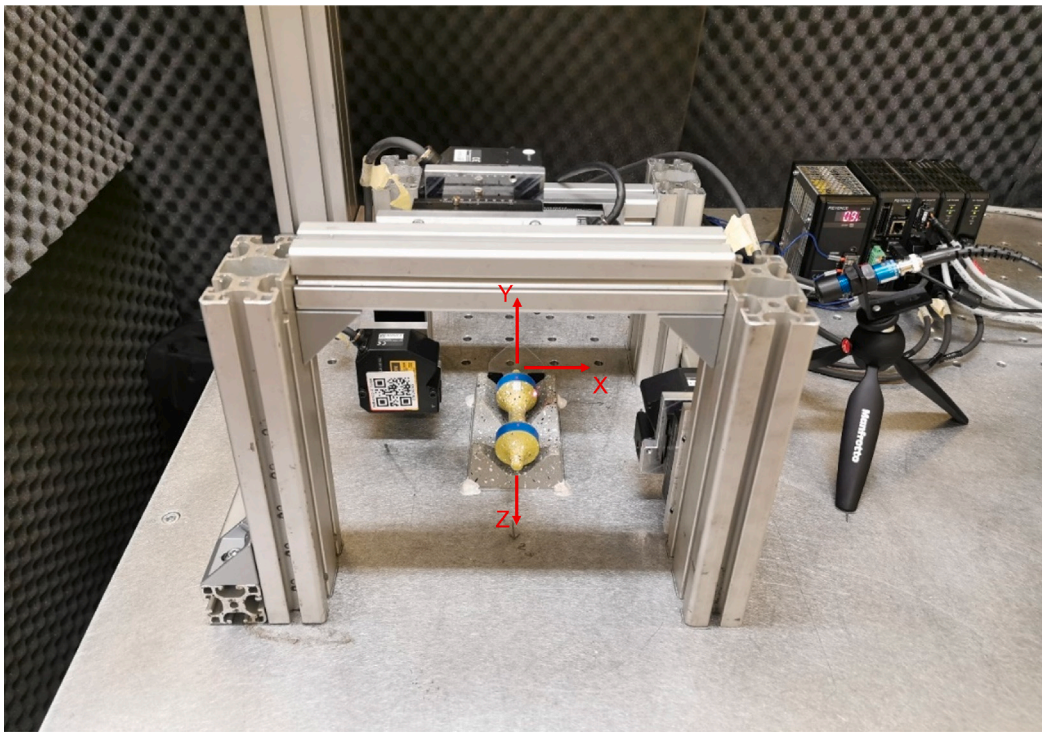

Fig. 2. Experimental setup.

Table 1
Material properties and geometric characteristics.

Type	Parameter	Value
Rotor	m, mass	44.5 g
	l, length	135 mm
	r, maximum radius	18.35 mm
	d, floating magnet – barycentre distance	35 mm
	I_d, diametrical mass moment of inertia	$5.85 \cdot 10^{-5}$ kg m^2
	I_p, polar mass moment of inertia	$7.48 \cdot 10^{-6}$ kg m^2
Fixed magnets	b_1, length (x direction)	22 mm
	b_2, width (y direction)	22 mm
	h, height (z direction)	11 mm
	B_r, residual magnetic induction	0.277 T
	ρ, density	4480 kg/m^3
Floating magnets	d_{int}, internal diameter	18 mm
	d_{ext}, external diameter	32 mm
	h_d, height (x direction)	5 mm
	B_r, residual magnetic induction	0.277 T
	ρ, density	4480 kg/m^3

Bosch profiles are used to mount four Keyence Laser sensors (LK-H052, LK-H082, and LK-H152) measuring rotor horizontal and vertical displacements in sections #1 and #2 discussed in Fig. 1. The Laser data is post-processed using the approach adopted in [20].

The laser tachometer LaserTach LT2 ICP from "The modal shop" is positioned beside the rotor to measure the rotor angular speed. The tachometer points at a small reflective adhesive placed on the rotor section #1 at each rotor turn. The passage detection is used to estimate rotor angular speed.

All the sensor data are collected by LMS SCADAS Mobile acquisition board at a sampling frequency of 8192 Hz and post-processed in Matlab® environment.

Two types of tests are performed:

- *Null rotor angular speed free response*: rotor free end non-null displacement initial condition is imposed and null rotor angular speed $\Omega = 0$ to estimate the system natural frequencies;
- *Rotor angular speed sweep down*: rotor free response to a non-null rotor angular speed $\Omega \neq 0$ to investigate the rotor dynamic behaviour and support nonlinearities.

3.1. Null rotor angular speed free response

Null rotor angular speed free response tests have been performed with the following test protocol. The rotor free end is brought in contact with the target metal plate in Fig. 3, while the other rotor end is in contact with the base glass plate. The rotor free end non-null initial displacements x_p, y_p and null initial speeds $\dot{x}_p$, $\dot{y}_p$ are imposed and the target metal plate is 20 mm retracted towards z direction. Then, the rotor free response is recorded.

The x_g, y_g rotor barycentre displacements and θ_x, θ_y rotor rotations are obtained by using the post-processing methodology adopted in [21] and further described in Appendix A.

The Fast Fourier Transform (FFT) time–frequency analysis is performed over the modulus of the typical complex composition of barycentre displacements $x_g + \mathrm{i}y_g$ to study the amplitude of the radial displacement of the rotor. Fig. 4 shows the FFT spectrogram result for the selected null rotor angular speed free response test. The x axis corresponds to the test time while the y axis to the frequency content in the investigated bandwidth. The yellow colour content is low in amplitude, while the red colour one is higher in amplitude, hence more significant.

The two horizontal lines at 4.5 Hz and 5 Hz are related to two system natural frequencies. Moreover, two horizontal lines at twice the previous frequency values (almost 9 Hz and 10 Hz) are visible. These frequency contents are superharmonics caused by the nonlinear magnetic support stiffness characteristics.

3.2. Rotor angular speed sweep down

The angular speed sweep down test is performed with a strict test protocol. An operator spins the rotor, that is left spinning with angular speed decay by dissipation. A time history of at least 350 s is recorded

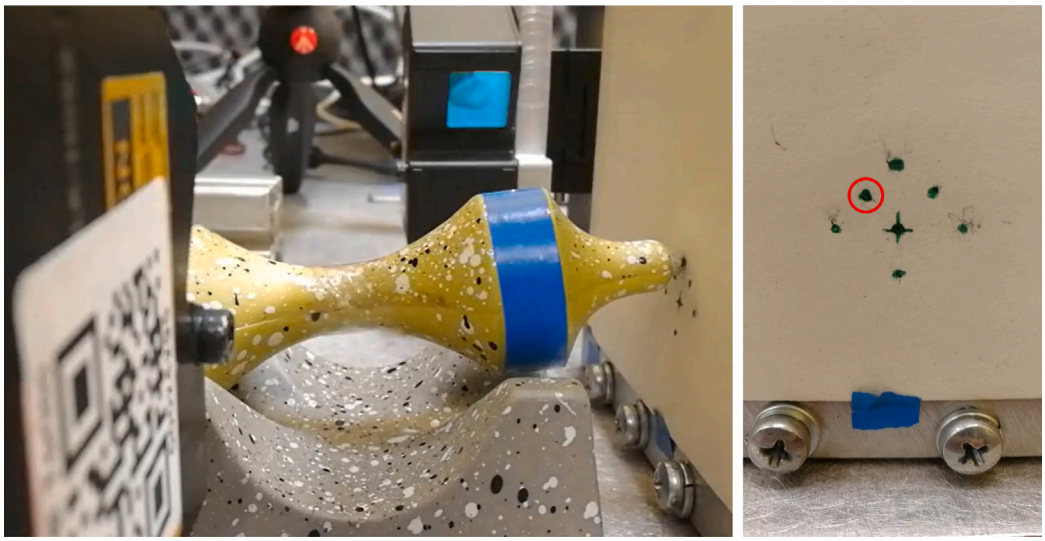

Fig. 3. Null rotor angular speed free response test: rotor free end lateral view (left), and initial condition of the analysed test (right).

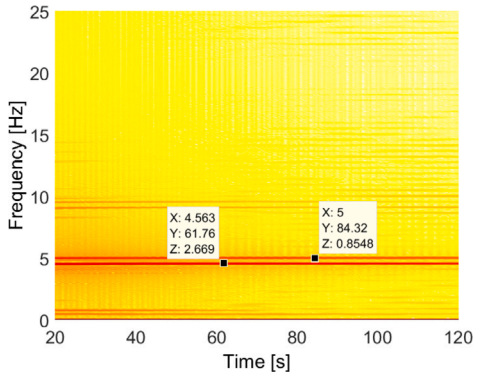

Fig. 4. Experimental FFT spectrogram of $|x_g + iy_g|$ (null angular speed). (For interpretation of the references to colour in this figure legend, the reader is referred to the web version of this article.)

to ensure the occurrence of resonance phenomena. Also, all the tests with measured rotor angular speed in the first 10 s below 1100 rpm are discarded.

The proposed test protocol is focused on the study of the dynamic behaviour of the system in different rotation regimes. Moreover, it is experimentally observed that the initial conditions only affect the initial transient behaviour, which is not of interest to this research. In fact, after the starting transient, being the rotor in supercritical regime, *i.e.*, the rotor self-centres, the initial conditions effects on the steady state behaviour are limited.

3.2.1. Time domain analysis

In this section, the Laser acquisitions are analysed and post-processed with Appendix A procedure to obtain the whole rotor axis trajectory.

In Fig. 5, the Laser measurements are shown. The rotor displacements exhibited at section #2 are wider than the ones at section #1, since the rotor oscillates around a centre of rotation which is between the contact point C and centre of magnet support S_1. The amplitude abrupt increments, up to 8 mm, are related to rotor resonances.

Also, resonance regimes can be identified in Fig. 6 at rotor angular speed drop time instants, respectively at 132 s and 195 s, which correspond to large amplitude behaviour and higher energy dissipation rate. The first resonance phenomenon occurs at a rotor angular speed of 580 rpm, while the second resonance occurs at about 290 rpm.

The developed experimental test-rig is devoted to the evaluation of angular speed in z direction only. Even though, the large rotor displacements in resonance induce a three-dimensional spatial variability in the angular velocity direction.

In the experimental test, the rotor naturally passes through three regimes: supercritical, resonance, and subcritical. In supercritical and subcritical regimes, the eccentricity arm angular speed is almost constantly out-of-phase or in-phase with the rotor angular speed. Since precession and revolution motions are synchronous, the period detection is not affected by spatial variability. Consequently, the mean spatial variability effect on the angular speed in z direction is null at each revolution. In resonance regime the eccentricity arm angular speed is in quadrature with the rotor angular speed.

Then, after a resonance occurs by reaching a critical speed, *i.e.*, at 132 s, the phase between eccentricity arm and rotor angular speed starts to vary. This phase transient affects the tachometer measurements: since precession and revolution speeds are different, the two motions are no longer synchronous and the period between two reflective speckle acquisitions is altered by the angular velocity spatial variability.

This phenomenon can be seen in Fig. 5 as a marginal scatter occurring from 132 s to 195 s: the scatter is reduced by the progressive self-centring before the reaching of the next critical speed at 195 s. This effect cannot be avoided, hence the laser tachometer is placed at the section #1, the closest to the contact point, to minimise it due to the smaller displacements. Consequently, Fig. 6 data only show amplitude fluctuation of the rotor angular speed at $150 \div 195$ s transient.

The rotor, at the end of its slowdown at 275 s in Fig. 6, stops rotating and begins to oscillate as a pendulum.

In Fig. 7, all the significant rotor point displacements C, S_1, G, S_2, and P are analysed and compared.

The fitted displacements show the rotor oscillation phenomenon is prominently conical, due to the monotonically crescent amplitude from the constraint to the free end.

Moreover, the figure shows a non-null rotor constraint point displacement x_c, y_c (green curves), not compliant with visual experimental outcomes. In this case, the fitting procedure is affected by the effective rotor geometry, which is not perfectly circular, at sections #1 and #2. The fitting procedure assumes a constant rotor radius, calculated as the average of the experimental values at different angular locations of sections #1 and #2. Therefore, the measurements are affected by a periodic offset proportional to the rotor rotation angle θ_z.

The post-processed rotor free end trajectories are compared with identified rotor trajectories via "Kinovea" video tracking tool, to validate the rotor trajectory fitting procedure. Fig. 8 shows the rotor free

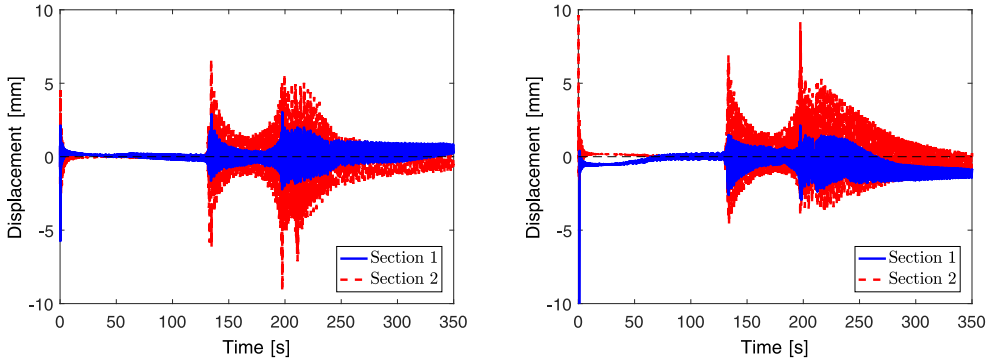

Fig. 5. Laser measurements of rotor x (left) and y (right) displacements. (For interpretation of the references to colour in this figure legend, the reader is referred to the web version of this article.)

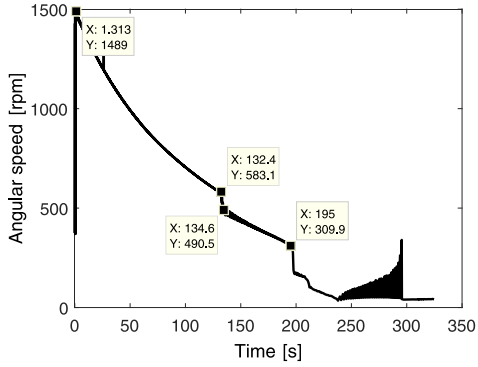

Fig. 6. Rotor angular speed.

end trajectory larger in x direction, therefore the global rotor rotation is prominent in the xz plane. Differently, Fig. 9 shows a more significant rotor free end trajectory in y direction, hence related to the global rotor rotation in the yz plane.

3.2.2. Frequency domain analysis

Time–frequency analysis is performed on post-processed Laser displacement data, by evaluating the radial amplitude $|x_g + \mathrm{i}y_g|$ frequency content during the rotor angular sweep down test. The FFT spectrogram is computed with a frequency resolution of 0.1 Hz, a compromise between time windows averaging and frequency content scattering.

The FFT spectrogram of Fig. 10 can be divided into four time history parts:

- *Supercritical regime and superharmonics* ($t = 0 \div 132$ s): the rotor shows small amplitudes of the natural frequency harmonics, *i.e.*, small orbit trajectories, since the rotor is in self-centring regime. Moreover, the descending trend curves are all related to the rotor angular speed Ω. The first harmonic Ω, *i.e.*, the lower descending curve, appears at the instantaneous rotor angular speed. Also higher order superharmonics are present, *i.e.*, the 2Ω, 3Ω, 4Ω, 5Ω descending curves at multiples of instantaneous rotor angular speed.
  In this system, the superharmonics are caused by the smooth nonlinearities of magnetic support stiffness characteristics [22,23]. Even superharmonics show higher amplitudes than the odd ones, since they are related to the asymmetric magnet configuration.
- *First resonance regime by subharmonics* ($t = 132 \div 195$ s): this regime begins when harmonics related to Ω cross the natural frequency horizontal lines. This resonance is explained by the subharmonic response effect of nonlinear phenomena, already investigated in various rotordynamics case studies [24–27]. Subharmonic vibration refers to the response of a dynamic system to the excitation at a whole-number multiple n of its natural frequency by vibrating asynchronously at its natural frequency at $1/n$ of the excitation.
- *Critical speed of first harmonic* ($t = 195 \div 275$ s): the first harmonic Ω crosses the two natural frequency curves at 195 s.
- *Amplitude decay up to pendulum motion* ($t = 275 \div 400$ s): in this time span the rotor regime passes from rotation to non-complete rotation oscillation as a pendulum.

4. Magnetic support modelling

The interactions between fixed and floating magnets are described via a continuous magnetic model developed in Matlab environment with LUPOS package [28]. The restoring force and torque mappings are evaluated by considering one floating magnet at time, discretely moved in y and x directions. Eq. (1) allows the evaluation of the generalised magnetic forces between the infinitesimal magnets 1 and 2 in Fig. 11 by considering the mutual magnetisation field $\mathbf{M}_1$ and the magnetic flux density $\mathbf{B}_2$ (or $\mathbf{M}_2$ and $\mathbf{B}_1$).

$$\begin{aligned}\mathbf{F}_{1\to2} &= \nabla\left(\mathbf{M}_2\cdot\mathbf{B}_1\right) = -\nabla\left(\mathbf{M}_1\cdot\mathbf{B}_2\right)\\ \mathbf{T}_{1\to2} &= \mathbf{M}_2\wedge\mathbf{B}_1 = \mathbf{M}_1\wedge\mathbf{B}_2\end{aligned} \tag{1}$$

The generalised force components of $\mathbf{F}_{1\to2}$ and $\mathbf{T}_{1\to2}$ are represented in Eq. (2) as directional derivatives of the magnetic flux density components.

$$\begin{aligned}F_{1\to2,x} &= -\left(M_{x,2}\frac{\partial B_{x,1}}{\partial x} + M_{y,2}\frac{\partial B_{x,1}}{\partial y} + M_{z,2}\frac{\partial B_{x,1}}{\partial z}\right)\\ F_{1\to2,y} &= -\left(M_{x,2}\frac{\partial B_{y,1}}{\partial x} + M_{y,2}\frac{\partial B_{y,1}}{\partial y} + M_{z,2}\frac{\partial B_{y,1}}{\partial z}\right)\\ T_{1\to2,x} &= M_{y,2}B_{z,1} - M_{z,2}B_{y,1}\\ T_{1\to2,y} &= M_{z,2}B_{x,1} - M_{x,2}B_{z,1}\end{aligned} \tag{2}$$

Therefore, Eq. (2) are integrated to obtain the generalised magnetic forces between the fixed and the floating magnets with Eq. (3).

$$\begin{aligned}\mathbf{F}_{fix\to float} &= -\int_{V,fix}\mathbf{M}_{fix}\cdot\nabla\mathbf{B}_{float}dV = \int_{V,float}\mathbf{M}_{float}\cdot\nabla\mathbf{B}_{fix}dV\\ \mathbf{T}_{fix\to float} &= \int_{V,fix}\mathbf{M}_{fix}\wedge\mathbf{B}_{float}dV = -\int_{V,float}\mathbf{M}_{float}\wedge\mathbf{B}_{fix}dV\end{aligned} \tag{3}$$

The generalised forces by concave, hollow, or complex volumes are obtained by linear superposition of prismatic convex volumes effects. In this application, the support magnets are modelled using rectangular prismatic shapes equivalent in volume to the real ones, considerably reducing the computational cost for the generalised force estimations. In this application, the generalised magnetic forces are calculated as functions of the floating magnet displacements (whose axial distance from the barycentre is d). These displacements are obtained as superposition of rotor barycentre translations epurated of static offsets at static equilibrium position $\bar{x}_g$, $\bar{y}_g$ and rotations θ_x and θ_y with Eq. (4).

$$\begin{aligned}\bar{x}_1 &= \bar{x}_g - d\sin\theta_y\\ \bar{y}_1 &= \bar{y}_g + d\sin\theta_x\\ \bar{x}_2 &= \bar{x}_g + d\sin\theta_y\\ \bar{y}_2 &= \bar{y}_g - d\sin\theta_x\end{aligned} \tag{4}$$

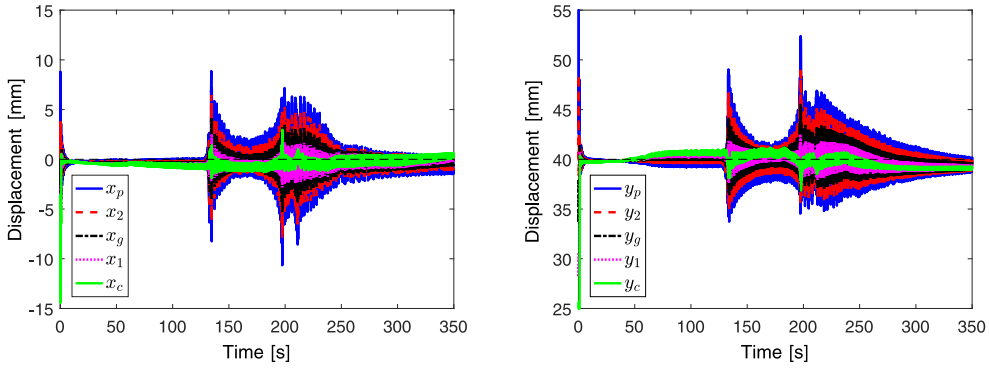

Fig. 7. Rotor fitted x (left) and y (right) displacements. (For interpretation of the references to colour in this figure legend, the reader is referred to the web version of this article.)

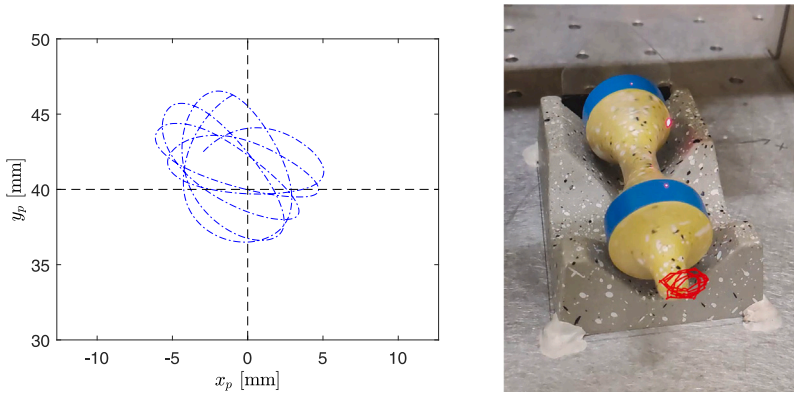

Fig. 8. Rotor free end P trajectory around first resonance ($t = 195$ s): post-processing (left) and video tracking (right).

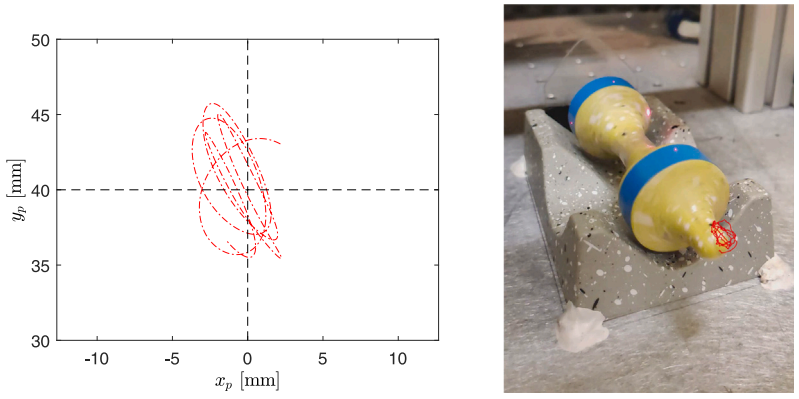

Fig. 9. Rotor free end P trajectory around second resonance ($t = 220$ s): post-processing (left) and video tracking (right).

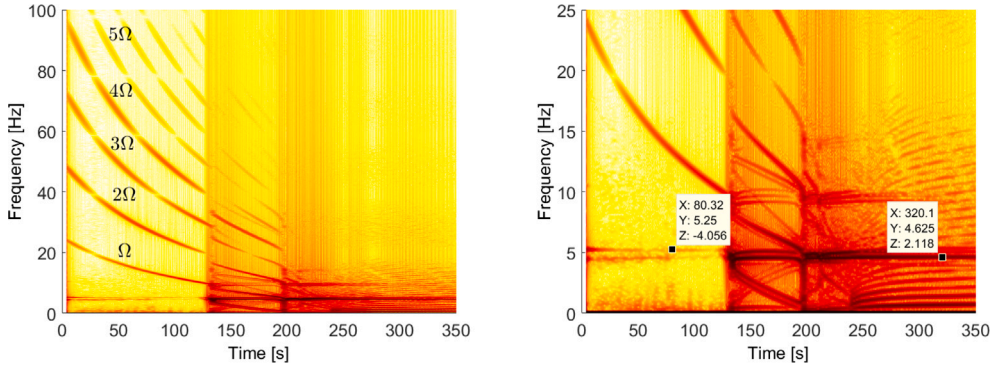

Fig. 10. Experimental FFT spectrogram of $|x_g + iy_g|$ (rotor angular speed sweep down) (left) and a detail (right).

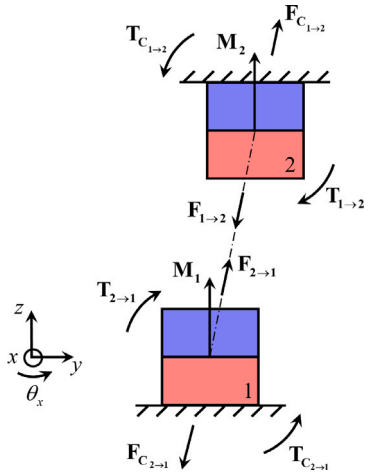

Fig. 11. Force and torque interactions between two magnets.

The computed generalised magnetic forces are shown in Figs. 12 and 13. In the maps, the floating magnet is moved in the range $[-15, 15]$ mm around the local rotor reference frame.

The maps show a switch trend from increasing to decreasing (and vice versa) when the floating magnet horizontal displacement value is close to ± 10 mm or when vertical displacement value is close to -10 mm. This behaviour is caused by interpenetration of floating and fixed magnets for those values of floating magnet displacement in the mapping. This condition, analytically computed, has no physical meaning, and is never reached by floating magnets during simulations.

The magnetic map shows the magnetic field as a function of the floating magnet motion under small oscillations hypothesis.

4.1. Magnetic characteristic approximation

The generalised magnetic force mappings, theoretically computed in the previous Section 4, are in this section analytically approximated by using Eq. (5), used in [29–31].

$$F_m = \frac{A}{\left(1 + \frac{x}{B}\right)^n} \tag{5}$$

where A, B, and n are empirical parameters depicting the magnetic force F_m. This passage is finalised to obtain generalised magnetic forces compact polynomial formulations, easily manageable in the linear model development described in Section 4.1.

Therefore, it is obtained:

$$\begin{aligned}
F_{m,x}(x,y) &= \frac{A_{F,xy}}{\left(1 + \frac{\bar{y}_z}{B_{F,xy}}\right)^{n_{F,xy}}} \left(\frac{A_{F,xx}}{\left(1 + \frac{\bar{x}_z}{B_{F,xx}}\right)^{n_{F,xx}}} - \frac{A_{F,xx}}{\left(1 - \frac{\bar{x}_z}{B_{F,xx}}\right)^{n_{F,xx}}} \right) \\
F_{m,y}(x,y) &= \frac{A_{F,yy}}{\left(1 + \frac{\bar{y}_z}{B_{F,yy}}\right)^{n_{F,yy}}} + \frac{A_{F,yx}}{\left(1 + \frac{\bar{x}_z}{B_{F,yx}}\right)^{n_{F,yx}}} + \frac{A_{F,yx}}{\left(1 - \frac{\bar{x}_z}{B_{F,yx}}\right)^{n_{F,yx}}} \\
T_{m,x}(x,y) &= \frac{A_{T,xy}}{\left(1 + \frac{\bar{y}_z}{B_{T,xy}}\right)^{n_{T,xy}}} + \frac{A_{T,xx}}{\left(1 + \frac{\bar{x}_z}{B_{T,xx}}\right)^{n_{T,xx}}} + \frac{A_{T,xx}}{\left(1 - \frac{\bar{x}_z}{B_{T,xx}}\right)^{n_{T,xx}}} \\
T_{m,y}(x,y) &= \frac{A_{T,yy}}{\left(1 + \frac{\bar{y}_z}{B_{T,yy}}\right)^{n_{T,yy}}} \left(\frac{A_{T,yx}}{\left(1 + \frac{\bar{x}_z}{B_{T,yx}}\right)^{n_{T,yx}}} - \frac{A_{T,yx}}{\left(1 - \frac{\bar{x}_z}{B_{T,yx}}\right)^{n_{T,yx}}} \right)
\end{aligned} \tag{6}$$

Table 2
Unbalance reference default value.

Parameter	Value
ε_{ref}, static unbalance	$4.3 \cdot 10^{-6}$ m
γ_{ref}, dynamic unbalance	$4.8 \cdot 10^{-3}$ rad

In Eq. (6), the $\bar{x}_z$ and $\bar{y}_z$ quantities generically refer to the directions of the evaluation of the generalised magnetic forces. In this application, the evaluation of Eq. (6) is limited to rotor floating magnet central points S_1 and S_2, therefore the subscript z is substituted with 1 and 2 in the complete model formulation.

The signs of forces and torques in Eq. (6) are defined by considering the restoring action of fixed magnets on floating magnets. Parameters A, B and n, listed in Table B.4, are evaluated by fitting polynomial force functional to the nonlinear magnetic force maps in Figs. 12 and 13. The same force fitting parameters are used to compute polynomial magnetic torques since both have the same surface shapes. Force fitting parameters are scaled by 10^{-3} factor.

5. Rotor model

The Jeffcott rotor model is taken as a starting reference to model this horizontal magnetic rotor. A common way to model magnetic coupling consists of using springs, as in [15,32,33], characterised by stiffness coefficients related to forces generated by the interactions between floating and fixed magnets. Stiffness terms can be linear or nonlinear depending on the type of the target behaviour. Fig. 14 shows a representation of the rotor model: the magnetic forces act on the respective floating magnet, the mass is considered lumped at the barycentre, the forces and torques are expressed with restoring convention. Moreover, the force directions orthogonal to the plane are represented with "$\odot$" and "$\otimes$" symbols. The "$\odot$" symbol represents an arrow that is coming out of the page and the "$\otimes$" symbol represents an arrow that is going into the page. Rotor systems are subject to excitation based on their angular speed, similarly to other systems subject to parametric excitation [34]. Since a real rotor is not perfectly axisymmetric, the barycentre is a point that does not belong to system axis, hence periodic forces created by eccentricity effect (7) must be considered.

$$\begin{aligned}
F_{\varepsilon_x} &= m\varepsilon\Omega^2 \cos(\Omega t) \\
F_{\varepsilon_y} &= m\varepsilon\Omega^2 \sin(\Omega t)
\end{aligned} \tag{7}$$

The proposed method to calculate the eccentricity by Eq. (8) consists of evaluating the period of oscillation T, hence its frequency ω_n, when the rotor stops rotating and begins to oscillate as a pendulum about its equilibrium position at the end of the time history of Fig. 6.

$$\omega_n = \sqrt{\frac{mg\varepsilon}{I_p}} \tag{8}$$

$$\varepsilon = \frac{I_p}{T^2 mg} \tag{9}$$

Since rotor mass is unevenly distributed around the rotation axis, its barycentre is out of alignment with the centre of rotation, so dynamic unbalance must be considered [35], and it generates an unbalance moment that is expressed as follows:

$$\begin{aligned}
T_{\gamma_x} &= \gamma\Omega^2 \left(I_p - I_d\right) \sin(\Omega t) \\
T_{\gamma_y} &= \gamma\Omega^2 \left(I_d - I_p\right) \cos(\Omega t)
\end{aligned} \tag{10}$$

Parametric analyses are performed to investigate the effect of static and dynamic unbalances on the dynamics of this magnetic rotor to obtain displacement amplitudes compliant with the experimental ones (see Table 2).

Furthermore, two more parametric analyses are performed with LUPOS software to model the contact between the glass plate and rotor

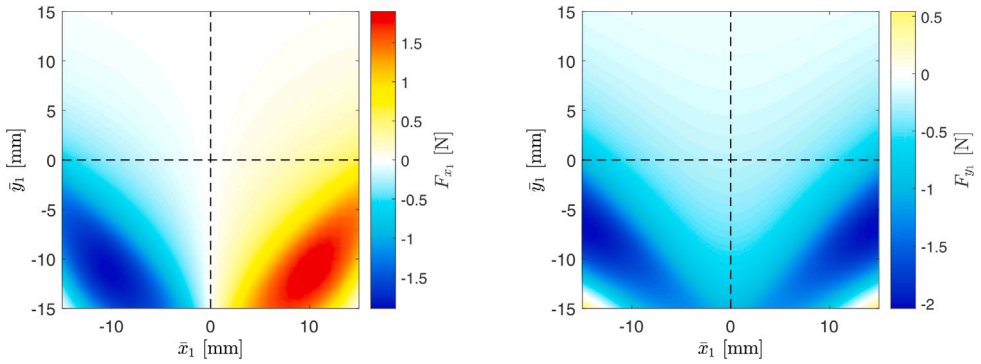

(a) Magnetic forces F_{x_1} (left) and F_{y_1} (right).

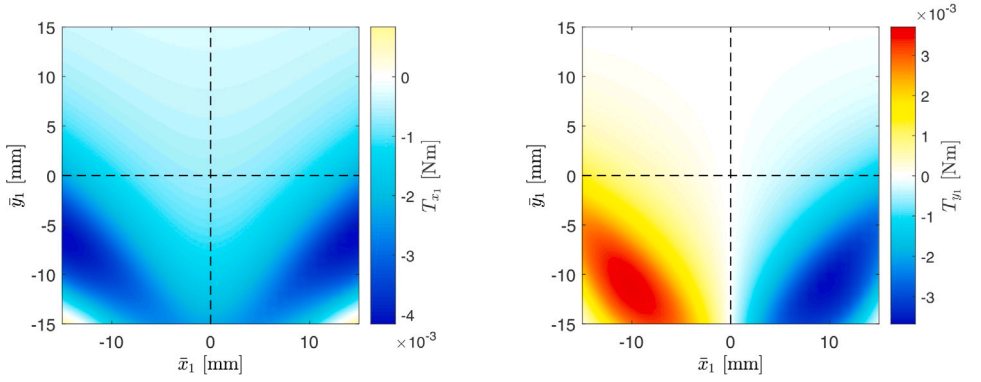

(b) Magnetic torques T_{x_1} (left) and T_{y_1} (right).

Fig. 12. Generalised magnetic forces at rotor support S_1. (For interpretation of the references to colour in this figure legend, the reader is referred to the web version of this article.)

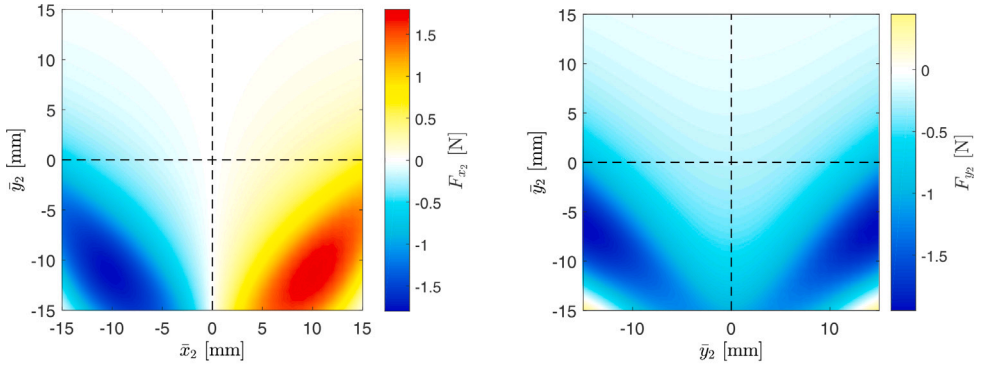

(a) Magnetic forces F_{x_2} (left) and F_{y_2} (right).

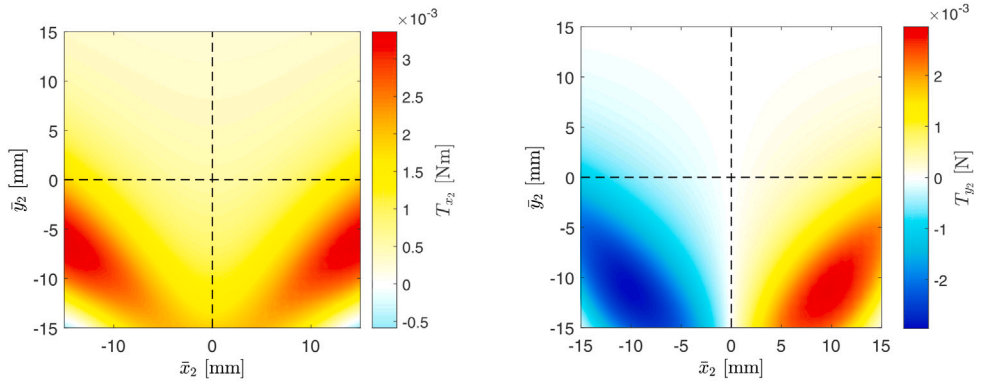

(b) Magnetic torques T_{x_2} (left) and T_{y_2} (right).

Fig. 13. Generalised magnetic forces at rotor support S_2. (For interpretation of the references to colour in this figure legend, the reader is referred to the web version of this article.)

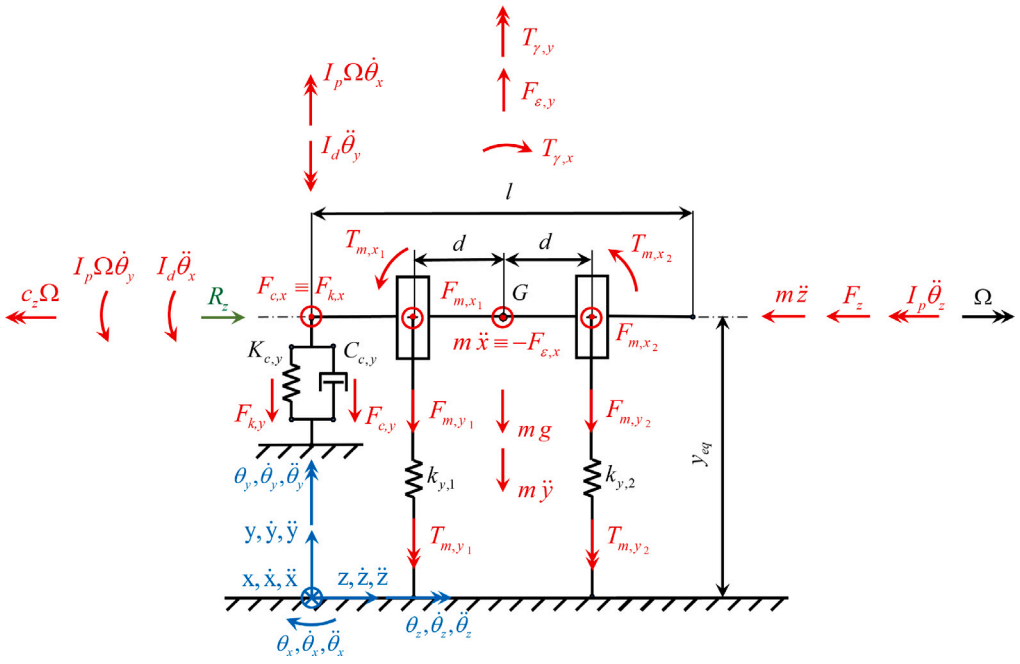

Fig. 14. Free body diagram of ideal rotor.

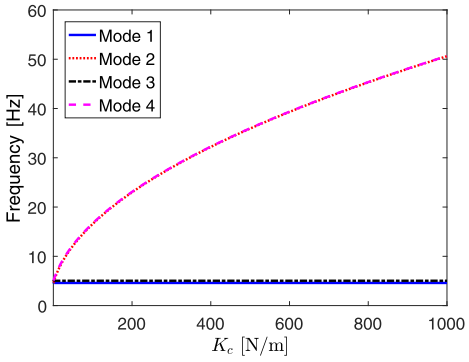

Fig. 15. Stiffness parametric analysis ($K_c = K_{c,x} = K_{c,y}$): mode frequencies.

constraint end, since considering it as a pinned constraint would delete the dynamic behaviour related to x and y degrees of freedom (DOF). Two possible options are evaluated:

- spring constraint;
- damper constraint.

Stiffness and damping are evaluated by simultaneously varying their respective x and y values, since a parametric analysis with null angular speed makes gyroscopic effects null and x and y DOFs result uncoupled. The first parametric analysis, whose result is shown in Fig. 15, is performed by analysing mode frequency variation while changing the values of the two stiffness terms $K_{c,x}$ and $K_{c,y}$ and keeping damping terms $C_{c,x}$ and $C_{c,y}$ null. Only the first four modes are investigated, ignoring rigid body motion and modes related to z translation and θ_z rotation.

Modes 2 and 4, related to x and y translations, are the ones more influenced by stiffness increase. Increasing the stiffness would hinge the rotor end as a pinned constraint, while rotor constrained tip drifts on the glass plate, as shown in Fig. 7. Hence, a second parametric analysis, whose results are shown in Fig. 16, is performed by investigating mode frequencies and damping ratio while changing the values of the two damping terms $C_{c,x}$ and $C_{c,y}$ and keeping stiffness terms $K_{c,x}$ and $K_{c,y}$ null.

The first eight complex and conjugate modes, excluding rigid body motion and modes related to z translation and θ_z rotation, are investigated. Similarly to the previous analysis, Fig. 16, the complex and conjugate modes 1, 2, 5, and 6, related to x and y translations, are more influenced by damping increase. In fact, from C_c values higher than 0.6 Ns/m they start to vary, while the other modes remain unaltered. Additionally, the latter modes become overdamped when $C_c = 0.6$ Ns/m. In conclusion, it is possible to obtain experimentally compliant dynamic behaviour by using a damping constraint equal to or higher than 0.6 Ns/m. Furthermore, the use of a damper instead of a spring allows an xy plane drift of the rotor end on the glass plate (as shown in Fig. 7).

For this application, $C_c = 2$ Ns/m even though displacements of the rotor end in contact with the glass plate are characterised by a variation which is smaller than the ones in the experimental case, as it can be seen comparing Fig. 16 to Fig. 7. The real behaviour is found more compliant with the simulated one by assuming this damping value.

5.1. Linearised model

In order to develop a linearised rotor model, it is necessary to calculate constant stiffness coefficients as derivatives of the generalised magnetic forces evaluated at the equilibrium position from Eq. (6). The main passages are shown in Appendix B. The linear model is expressed as the following matrix system:

$$\mathbf{M}\ddot{\mathbf{x}} + (\mathbf{C} + \Omega\mathbf{G})\,\dot{\mathbf{x}} + \mathbf{K}\mathbf{x} = \mathbf{F} \tag{11}$$

where:

$$\mathbf{x} = \left\{ x \quad \bar{y} \quad z \quad \theta_x \quad \theta_y \quad \theta_z \right\}^T \tag{12}$$

$$\mathbf{M} = \begin{bmatrix} m & 0 & 0 & 0 & 0 & 0 \\ 0 & m & 0 & 0 & 0 & 0 \\ 0 & 0 & m & 0 & 0 & 0 \\ 0 & 0 & 0 & I_d & 0 & 0 \\ 0 & 0 & 0 & 0 & I_d & 0 \\ 0 & 0 & 0 & 0 & 0 & I_p \end{bmatrix} \tag{13}$$

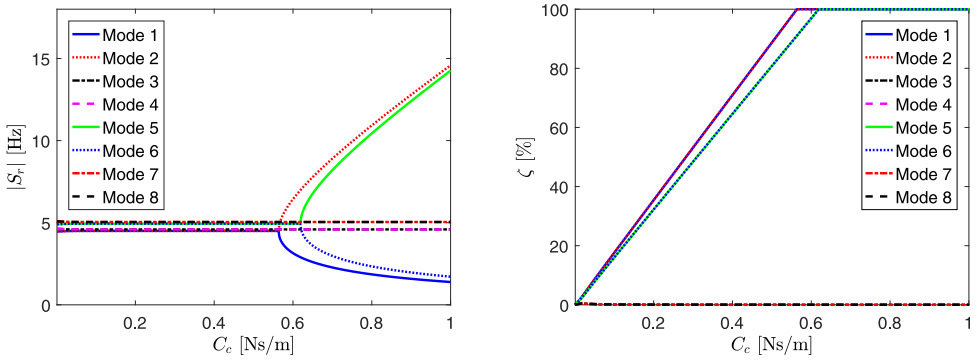

Fig. 16. Damping parametric analysis ($C_c = C_{c,x} = C_{c,y}$): pole modulus (left) and damping ratio (right).

Table 3
Simulation initial conditions.

Parameter	Ω, angular speed	$\mathbf{x}$, DOF vector	$\dot{\mathbf{x}}$, DOF derivative vector
Value	157 rad/s	$\{10^{-5}\ \text{m}, 10^{-5}\ \text{m}, 0\ \text{m}, 10^{-5}\ \text{rad}, 10^{-5}\ \text{rad}, 0\ \text{rad}\}$	$\{0.1\ \text{m/s}, 0.1\ \text{m/s}, 0\ \text{m/s}, 0.3\ \text{rad/s}, 0.3\ \text{rad/s}, 157\ \text{rad/s}\}$

$$\mathbf{C} = \begin{bmatrix} C_{c,x} & 0 & 0 & 0 & -C_{c,x}\frac{l}{2} & 0 \\ 0 & C_{c,y} & 0 & C_{c,y}\frac{l}{2} & 0 & 0 \\ 0 & 0 & 0 & 0 & 0 & 0 \\ 0 & C_{c,y}\frac{l}{2} & 0 & C_{c,y}\frac{l^2}{4}+C & 0 & 0 \\ -C_{c,x}\frac{l}{2} & 0 & 0 & 0 & C_{c,x}\frac{l^2}{4}+C & 0 \\ 0 & 0 & 0 & 0 & 0 & C_{\Omega} \end{bmatrix} \tag{14}$$

$$\mathbf{G} = \begin{bmatrix} 0 & 0 & 0 & 0 & 0 & 0 \\ 0 & 0 & 0 & 0 & 0 & 0 \\ 0 & 0 & 0 & 0 & 0 & 0 \\ 0 & 0 & 0 & 0 & I_p & 0 \\ 0 & 0 & 0 & -I_p & 0 & 0 \\ 0 & 0 & 0 & 0 & 0 & 0 \end{bmatrix} \tag{15}$$

$$\mathbf{K} = \begin{bmatrix} K_{F_x,x} & K_{F_x,y} & 0 & K_{F_x,\theta_x} & K_{F_x,\theta_y} & 0 \\ K_{F_y,x} & K_{F_y,y} & 0 & K_{F_y,\theta_x} & K_{F_y,\theta_y} & 0 \\ 0 & 0 & K_{F_z,z} & 0 & 0 & 0 \\ K_{T_x,x} & K_{T_x,y} & 0 & K_{T_x,\theta_x} & K_{T_x,\theta_y} & 0 \\ K_{T_y,x} & K_{T_y,y} & 0 & K_{T_y,\theta_x} & K_{T_y,\theta_y} & 0 \\ 0 & 0 & 0 & 0 & 0 & 0 \end{bmatrix} \tag{16}$$

$$\mathbf{F} = \begin{Bmatrix} F_{\varepsilon_x} & F_{\varepsilon_y} & R_z & T_{\gamma_x} & T_{\gamma_y} & 0 \end{Bmatrix}^T \tag{17}$$

C terms added to $\mathbf{C}$ Coulomb friction matrix [36], correspond to dummy dampers acting on rotational DOFs to simulate rotordynamics. The term C_Ω is tuned to create a speed sweep down compliant with the experimental one. Displacements caused by x and y translational DOFs are already damped by the constraint dummy damper, so it is not necessary to add more C terms to the $\mathbf{C}$ matrix. To tune these C damping terms, it is necessary not to overcome $\Omega\mathbf{G}$ terms so as not to hide the gyroscopic effect. For this application, C damping parameter is $5 \cdot 10^{-5}$ N ms/rad. The developed linear model is used to simulate the angular speed sweep down of the system. The simulation initial conditions are listed in Table 3.

The parameters of Table 3 are chosen to start the simulation with non-null conditions applied to each DOF but the ones related to z and θ_z. Furthermore, starting damping parameters of 0.1 Ns/m and 0.1 N ms/rad are applied to the system during the first 5 s of the simulation to limit the rotor dynamics dependence from the initial conditions and facilitating the system reaching of operating conditions.

5.1.1. Time domain analysis

The linear model results are presented in Fig. 17 to highlight limits and advantages of the linearisation of this specific case study characterised by nonlinearities.

The starting anomalous displacements of Fig. 17 are caused by the starting damping. The main differences between the linear model displacements and the experimental ones are:

- *Lack of the first resonance phenomenon at* 132 s: the first experimental resonance is due to the subharmonic resonance effect, described in Section 3.2.2, hence it cannot be shown by the linear model. Actually, the linearisation of the generalised magnetic forces removes all high order contributions causing superharmonics and subharmonics seen in FFT spectrogram of Fig. 19.
- *DOFs decoupling*: the linearisation of magnetic maps causes decouples DOFs, since all the cross-derivatives are null. Therefore, high displacements in resonance regime do not cause any variation of magnetic force on orthogonal directions. The two numerical resonances at 195 s and 220 s, are independent.
- *Incompatible orbit trajectories*: in the model yz plane displacement a small variation of the rotor behaviour occurs at 195 s as a consequence of the resonance in xz plane. This effect is caused by gyroscopic terms which weakly couple the rotational DOFs θ_x and θ_y. Again, the decoupling in the linear model is confirmed by the respective displacements from Fig. 17. Furthermore, by comparing the linear model orbit trajectories at the critical speeds (Fig. 18) with experimental test ones (Figs. 8 and 9), it is possible to observe that the linear model trajectories are symmetric with respect to x and y directions. Since the magnet configuration of the real system is not symmetric with respect to y direction, the related magnetic characteristics cannot be totally modelled by a linear map. On the other hand, the magnetic behaviour on the xz plane, where magnet positions are symmetric with respect to the origin of the reference system, can be properly simulated by linear stiffness.

5.1.2. Frequency domain analysis

The linear model time–frequency analysis is shown in Fig. 19. The FFT spectrogram does not show multiples of the fundamental harmonic related to rotor angular speed and of the two natural frequencies. Nevertheless, the model natural frequencies are close to the experimental ones. Additionally, the amplitudes of the whole FFT spectrogram are quite similar to the experimental ones, suggesting a dynamic behaviour of the linear model compliant with the experimental data.

Despite the highlighted differences, the results demonstrate how the linear model approximation is enough to simulate the overall rotor dynamic behaviour despite its nonlinearities.

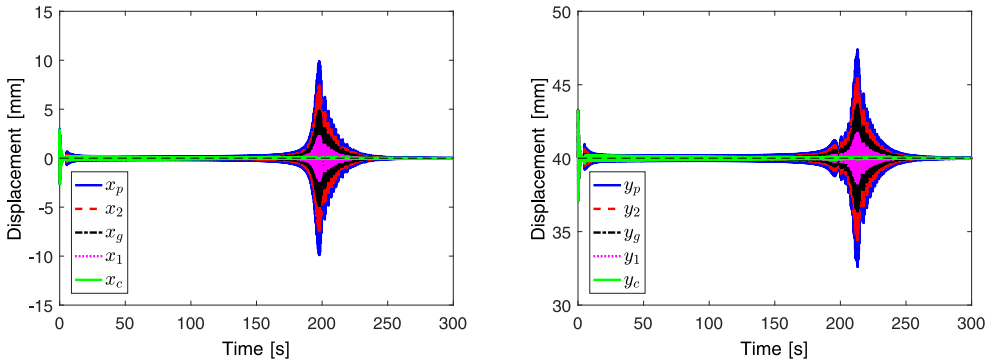

Fig. 17. Linear model rotor x (left) and y (right) displacements. (For interpretation of the references to colour in this figure legend, the reader is referred to the web version of this article.)

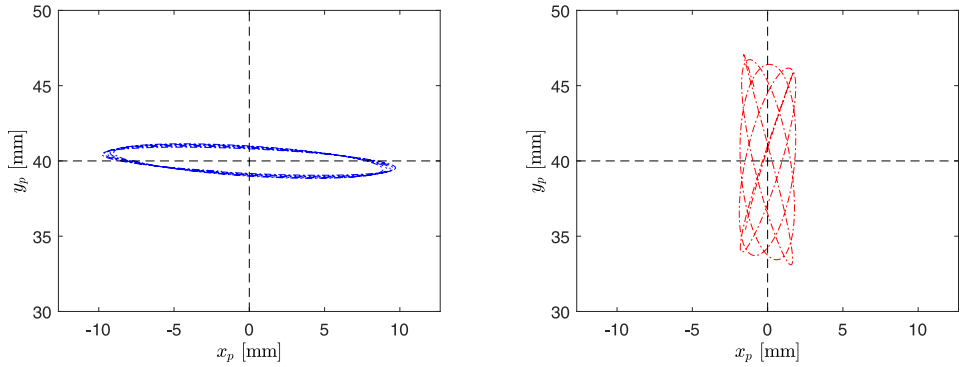

Fig. 18. Linear model rotor free end trajectories around resonances: $t = 195$ s (left) and $t = 220$ s (right).

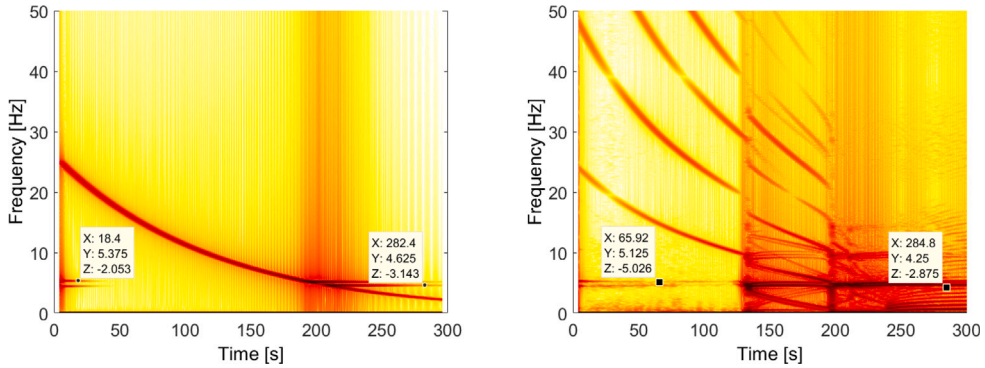

Fig. 19. Linear model (left) and experimental (right) FFT spectrograms.

5.2. Nonlinear model

A nonlinear model based on Eq. (18) is developed to thoroughly investigate the rotordynamics. The generalised magnetic force maps shown in Figs. 12 and 13 are used to model the nonlinear restoring force effect of the supports [37]. This nonlinear model can be expressed in matrix form as follows:

$$\mathbf{M}\ddot{\mathbf{x}} + (\mathbf{C} + \Omega\mathbf{G})\,\dot{\mathbf{x}} + \mathbf{F}_{nl} = \mathbf{F} \tag{18}$$

where $\mathbf{F}_{nl}$ is the nonlinear generalised force vector obtained from magnetic maps as functions of floating magnet positions.

$$\mathbf{F}_{nl} = \begin{Bmatrix} F_{m,x_1} + F_{m,x_2} \\ F_{m,y_1} + F_{m,y_2} \\ F_{m,z_1} + F_{m,z_2} \\ T_{m,x_1} + T_{m,x_2} + F_{m,y_1} d - F_{m,y_2} d \\ T_{m,y_1} + T_{m,y_2} - F_{m,x_1} d + F_{m,x_2} d \\ 0 \end{Bmatrix} \tag{19}$$

$$\mathbf{F} = \begin{Bmatrix} F_{\epsilon_x} & -mg + F_{\epsilon_y} & R_z & T_{\gamma_x} & T_{\gamma_y} & 0 \end{Bmatrix}^T \tag{20}$$

The same initial parameters and rotor angular speed profile as in Table 3 are used to simulate the rotor speed sweep down.

5.2.1. Time domain analysis

The nonlinear model results are presented in Fig. 20 to investigate the improvements of switching from the linear formulation to the respective nonlinear one.

Concerning the linear model limits highlighted in Section 5.1, the use of the nonlinear model allows for the following results:

- *Lack of the first couple of resonances*: there are no resonances but the couple at about 200 s;
- *DOF decoupling*: the second resonance causes wide displacements on yz plane and just a narrow displacement variation in xz plane;

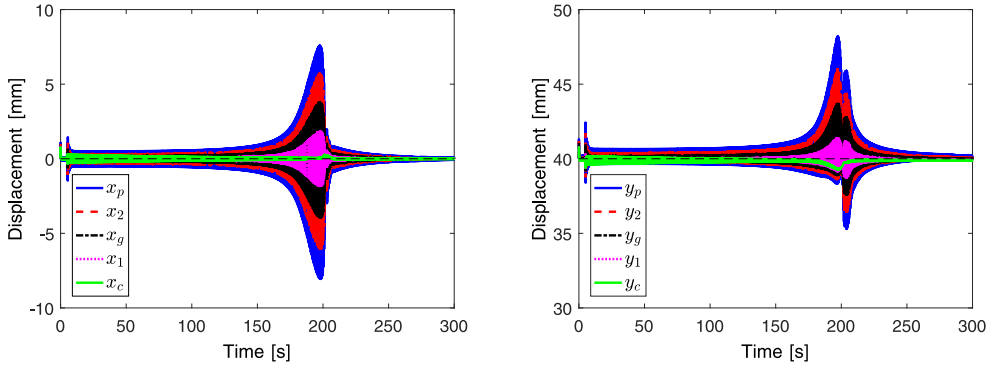

Fig. 20. Nonlinear model rotor x (left) and y (right) displacements. (For interpretation of the references to colour in this figure legend, the reader is referred to the web version of this article.)

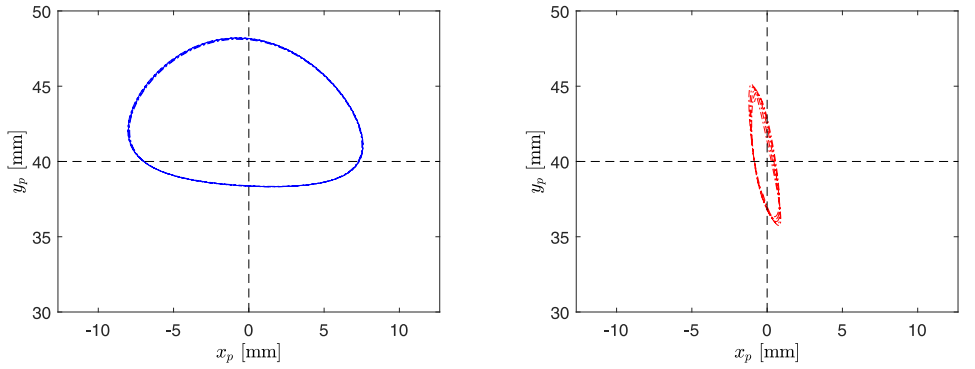

Fig. 21. Nonlinear model rotor free end trajectories around resonances: $t = 195$ s (left) and $t = 220$ s (right).

- *Compatible orbit trajectories*: the nonlinear model trajectories analysed in Fig. 21 are close to the experimental ones. In fact, the first resonance investigation shows a horizontally wide ovoid trajectory with a y average displacement higher than the equilibrium position, while the second resonance variation corresponds to a narrower vertical trajectory.

The ovoid trajectory can be analytically explained starting from the analytical model of the Jeffcott rotor with anisotropic supports [38]. This model assumes that, under the hypothesis of a reference system with the rotor axis in the z direction, supports can be modelled with different support stiffness K_x and K_y in the two directions causing an elliptical precession orbit. In the studied case, the orbit is not perfectly elliptical since, assuming the y direction to be vertical and orthogonal to the rotor axis, the support stiffness K_y is different between the parts above and below the rotor. A higher value of upward displacement in y direction corresponds to a lower value of Ky and, consequently, the ovoid trajectory in Fig. 21. The presence of the superharmonics in time–frequency analysis of Fig. 22 shows a further improvement of the nonlinear model if compared to the linear one.

The lack of the subharmonic resonance effect and the weak plane couplings are due to the way how magnetic forces and torques are calculated, as demonstrated in the following section.

5.3. Model updating

Traditionally, model updating for dynamics is performed by eigensensitivity optimisation based on structural parameter uncertainties [39] or by direct structural parameter updating against modal matrix with physical constraints [40]. In this application, the dependency of gyroscopic effects from rotor angular speed and model intrinsic nonlinearity makes the application of these procedures unfeasible. Therefore, the generalised magnetic force maps are tuned by multiplying them by parameters which change their shapes to highlight nonlinear characteristics. The aim of this procedure is to demonstrate how subharmonic resonance effect and DOFs coupling mainly depend on magnetic interaction. Each row of points of the maps, from the centre to the edge of the grid, is multiplied by a vector of rising values:

- $F_{m,x}$ by powers of 3 of the equally spaced vector $[1.1, \dots, 1.2]$;
- $F_{m,y}$ by powers of 2 of the equally spaced vector $[1.1, \dots, 1.4]$.

The choice to use different powers is made since $F_{m,y}$ and $T_{m,x}$ formulations should be more affected by an increment of their value which is closely related to the powers of even order, due to the vertical asymmetric configuration of the magnets. While, on the other hand, $F_{m,x}$ and $T_{m,y}$ formulations should be more affected by an increment of their value which is closely related to the powers of odd order, due to the horizontal symmetric configuration of the magnets. The two equally spaced vectors are different, since the objective is to multiply maps by a series of values whose maximum power (of different order) is the same. This process changes the natural frequency values, but it is not considered an issue since the tuning is not finalised to create a more accurate model and it is just a demonstration of the previous nonlinear model limits. The same initial parameters and angular speed profile of Table 3 are used to simulate the rotor speed sweep down.

Figs. 23 and 24 show the system behaviour with the applied modifications is even closer to the real one. DOFs are now coupled, even superharmonics are more evident than odd ones, and now the system shows the first resonance couple. Fig. 24, at the time interval from $100 \div 135$ s, shows the corresponding subharmonic resonance induced by even superharmonics. In fact, as the experimental first resonance, it starts when the main harmonic Ω assumes values equal to multiples of the main natural frequencies at 5 Hz and 6 Hz. These results confirm that the main approximation that causes the not total compliance of the original nonlinear model is due to the way how forces and torques are calculated. Therefore, the possible reason could be found in the estimation of these magnetic maps by just translating floating magnets instead of rotating them.

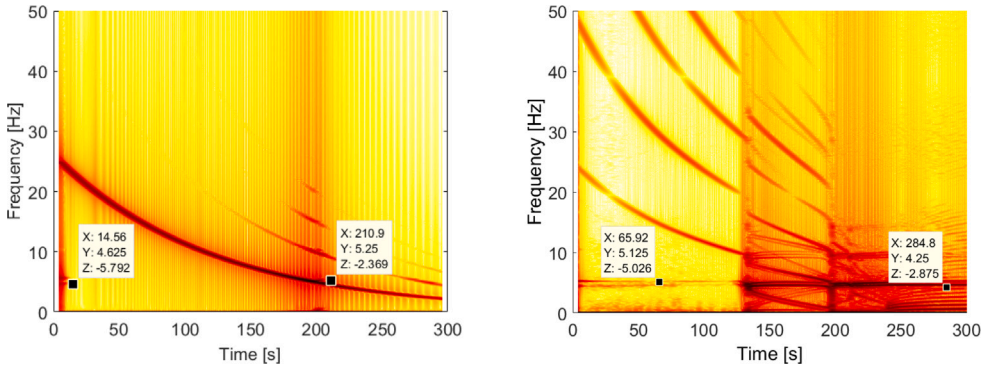

Fig. 22. Nonlinear model (left) and experimental (right) FFT spectrograms.

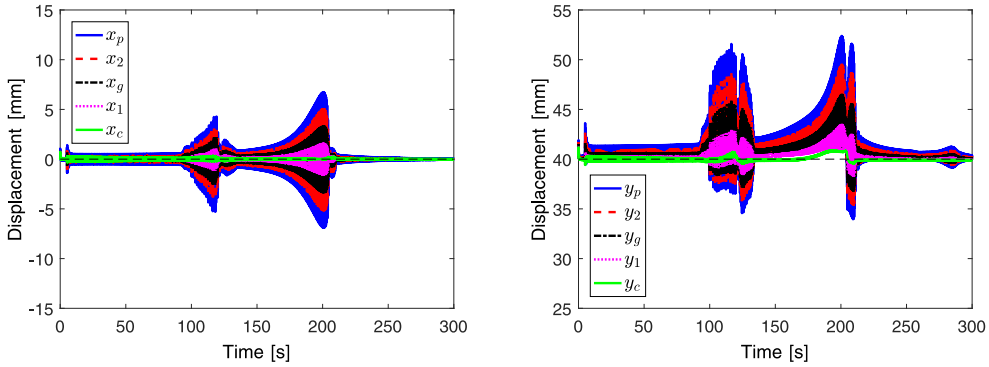

Fig. 23. Nonlinear tuned model rotor x (left) and y (right) displacements. (For interpretation of the references to colour in this figure legend, the reader is referred to the web version of this article.)

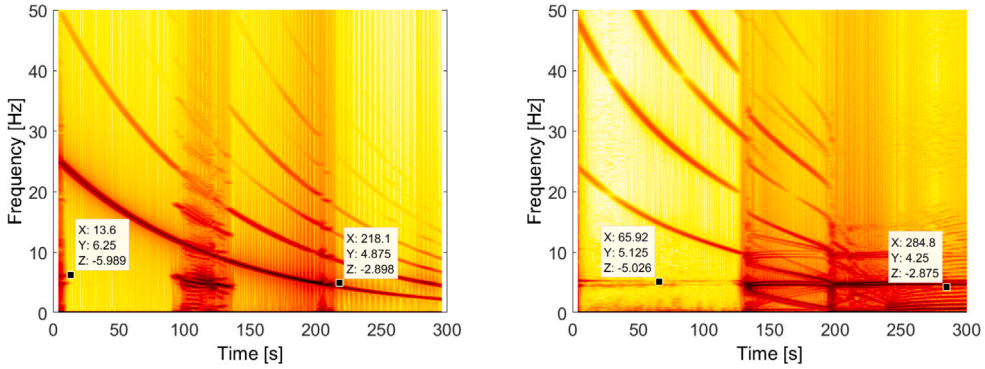

Fig. 24. Nonlinear tuned model (left) and experimental (right) FFT spectrograms.

6. Conclusions

The comparison between simulation results and experimental outcomes, shows that the approach proposed in this paper as methodology to develop models to simulate and analyse rotordynamics, is viable for quasi-conservative rotor systems characterised by smooth nonlinear passive supports.

Additionally, the analysed models can easily suit different rotor configurations, with appropriate modifications to the described analytical formulations. Finally, it is demonstrated how the main characteristics of the nonlinear system can be related to a linear model, which is indeed the one that most influences the rotordynamics. In fact, the developed linear model shows it is not necessary to add the nonlinear characterisation to obtain the correct natural frequencies and the overall understanding of the system dynamics.

It is necessary to use the nonlinear model if the objective of the analysis is to simulate a more accurate rotordynamics concerning trajectories and DOFs coupling, displacements, subharmonic and superharmonic effects. Indeed, the analysed results show how the nonlinear model, even with approximated magnetic maps, gives results compliant with the experimental outcomes. Despite that, it must be considered that the lack of subharmonic resonances represents a not negligible difference between the model and the real rotor. Consequently, considering just the nonlinear model itself, without an experimental reference, could lead to unexpected resonances of the system.

A future improvement concerning the experimental setup consists of using more sensors to perform displacement measurements of specular points at the two highlighted sections. In this way it is possible to exploit all the detected data to obtain an average value of fitted axis

position that is less affected by the not perfect axisymmetry of the rotor. Finally, as future development of this activity, it is straightforward to assume this approach, developed by analysing the educational demonstrator, as a tool to study the dynamics of similar configurations with magnetic bearings, as the ones of kinetic energy accumulators.

CRediT authorship contribution statement

Salvatore Paolo Cavallaro: Data curation, Formal analysis, Methodology, Software, Validation, Writing – original draft, Writing – review & editing. **Simone Venturini:** Data curation, Methodology, Software, Supervision, Visualization, Writing – original draft, Writing – review & editing. **Elvio Bonisoli:** Conceptualization, Funding acquisition, Project administration, Resources, Supervision, Visualization.

Declaration of competing interest

The authors declare that they have no known competing financial interests or personal relationships that could have appeared to influence the work reported in this paper.

Data availability

Data will be made available on request.

Acknowledgements

This paperwork is dedicated to the memory of prof. Elvio Bonisoli, a mentor, and a friend, who contributed to the result achievement of this project.

This publication is part of the project PNRR-NGEU which has received funding from the MUR – DM 351/2022.

The project is funded under the National Recovery and Resilience Plan (NRRP), Mission 4 Component 2 Investment 1.3 - Call for tender No. 1561 of 11.10.2022 of Ministero dell'Università e della Ricerca (MUR); funded by the European Union – NextGenerationEU, PE0000021, "Network 4 Energy Sustainable Transition – NEST".

Appendix A. Rotor axis trajectory fitting procedure

The procedure described in this section allows the evaluation of the axis position of a cylinder with a known radius, in a three-dimensional reference system, by using the coordinates of four points detected on its surface. Fig. A.25 shows the considered reference system. The rotor axis at the equilibrium condition corresponds to the z axis. The two couples of optical sensors provide displacement measurements of the points on the rotor surface at the two axial positions which correspond to sections #1 and #2 of Fig. 1. From the displacement of these points, acquired during the motion of the rotor, it is possible to determine two conics lying on the two planes corresponding to the two analysed sections.

The section of the cylinder at the analysed plane changes from a circumference to an ellipse due to the rotor motion. The transformation matrix $\mathbf{R}$ in Eq. (A.1) is used to obtain, from these two conics, the equations showing the position of the circular undeformed rotor sections in 3D space, and therefore the position of the rotor axis itself.

$$\mathbf{R} = \begin{bmatrix} 1 & 0 & 0 \\ 0 & \cos\theta_x & -\sin\theta_x \\ 0 & \sin\theta_x & \cos\theta_x \end{bmatrix} \begin{bmatrix} \cos\theta_y & 0 & \sin\theta_y \\ 0 & 1 & 0 \\ -\sin\theta_y & 0 & \cos\theta_y \end{bmatrix} \tag{A.1}$$

It is assumed to study a generic cylinder with its axis in z direction at equilibrium. The following three vectors (3×1) are defined:

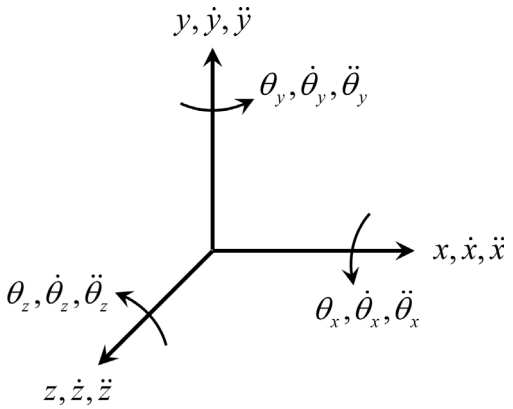

Fig. A.25. Reference system.

- $\boldsymbol{x}'$ post processed x', y', and z' coordinates of the points of the undeformed circumference with respect to the fixed global reference system.
- $\boldsymbol{x}$ experimental x, y, and z coordinates of the points measured by the optical sensors at the two planes where a section of the rotated and translated cylinder is detected.
- $\boldsymbol{\Delta x}$ translations in Δx, Δy, and Δz directions.

By considering the superposition of rotations and translations in Eq. (A.2) and the rotor section geometry with Eq. (A.3), the Eq. (A.4) is obtained:

$$\mathbf{x}' = \mathbf{R}^{\mathbf{T}} (\mathbf{x} - \mathbf{\Delta x}) \tag{A.2}$$

$$x'^2 + y'^2 = r^2 \tag{A.3}$$

$$a_9 x^2 + a_8 y^2 + a_7 z^2 + a_6 xy + a_5 xz + a_4 yz + a_3 x + a_2 y + a_1 z + a_0 = 0 \tag{A.4}$$

The parameters a_i are functions of the four unknown variables consisting of axis rotations θ_x, θ_y and translations Δx, Δy at the axial coordinate $z = 0$. The measured sets of point coordinates are four, as the number of the test-rig optical sensors. Therefore, it is possible to calculate the four previous unknowns from the following system written in matrix form:

$$\mathbf{Xa} = \mathbf{c} \tag{A.5}$$

where:

$$\mathbf{X} = \begin{bmatrix} x_1^2 & y_1^2 & z_1^2 & x_1 y_1 & x_1 z_1 & y_1 z_1 & x_1 & y_1 & z_1 \\ \vdots & \vdots & \vdots & \vdots & \vdots & \vdots & \vdots & \vdots & \vdots \\ x_4^2 & y_4^2 & z_4^2 & x_4 y_4 & x_4 z_4 & y_4 z_4 & x_4 & y_4 & z_4 \end{bmatrix} \tag{A.6}$$

where the coordinate subscript indicates the corresponding measured point. Axial coordinates z are the only ones that do not vary because they depend on the mounting position of the optical sensors.

$$\mathbf{a} = \begin{Bmatrix} \cos^2\theta_y \\ \sin^2\theta_x \sin^2\theta_y + \cos^2\theta_x \\ \cos^2\theta_x \sin^2\theta_y + \sin^2\theta_x \\ 2\cos\theta_y \sin\theta_x \sin\theta_y \\ -2\cos\theta_y \cos\theta_x \sin\theta_y \\ -2\left(\sin\theta_x \sin^2\theta_y \cos\theta_x - \cos\theta_x \sin\theta_x\right) \\ -2\left(\Delta x \cos^2\theta_y + \Delta y \cos\theta_y \sin\theta_x \sin\theta_y\right) \\ -2\left[\Delta x \cos\theta_y \sin\theta_x \sin\theta_y + \Delta y \left(\sin^2\theta_x \sin^2\theta_y + \cos^2\theta_x\right)\right] \\ 2\left[\Delta x \cos\theta_y \cos\theta_x \sin\theta_y + \Delta y \left(\sin\theta_x \sin^2\theta_y \cos\theta_x - \cos\theta_x \sin\theta_x\right)\right] \end{Bmatrix} \tag{A.7}$$

$$\mathbf{c} = \begin{Bmatrix} 1 & 1 & 1 & 1 \end{Bmatrix}^T [r^2 - \Delta x^2 \cos^2\theta_y \\ -\Delta y^2 \left(\sin^2\theta_x \sin^2\theta_y + \cos^2\theta_x\right) \\ -2\Delta x \Delta y \cos\theta_y \sin\theta_x \sin\theta_y] \tag{A.8}$$

Table B.4
Magnetic surface parameters.

Parameter	A [N]	B [m]	n [−]
$xx,1$	0.100000	0.150000	8.000000
$xy,1$	3.500000	0.124970	8.000000
$yx,1$	0.035523	0.092261	12.00000
$yy,1$	0.147200	0.112770	8.000000
$xx,2$	0.100000	0.138090	8.000000
$xy,2$	3.500000	0.125860	8.000000
$yx,2$	0.039148	0.093603	11.00000
$yy,2$	0.139900	0.112810	8.000000

The barycentre coordinates x_g and y_g can be evaluated during the whole time history with Eq. (A.9) after solving the system in Eq. (A.5) with the four sets of point coordinates at each time instant of the experimental test.

$$\begin{aligned} x_g &= x_{eq} + \Delta x + l/2 \sin\theta_y \\ y_g &= y_{eq} + \Delta y - l/2 \sin\theta_x \end{aligned} \tag{A.9}$$

where l is the length of the analysed rotor (see Table 1), and x_{eq} and y_{eq} respectively correspond to the horizontal and vertical offsets at the equilibrium position with respect to the reference system.

Appendix B. Magnetic interaction analytical formulation

The parameters used for the analytical formulation of the magnetic maps are shown in Table B.4.

The analytical model is developed from Eq. (B.1) referred to Fig. 14.

$$\begin{aligned} &m\ddot{x} + F_{m,x_1} + F_{m,x_2} + F_{c,x} = F_{\varepsilon_x} \\ &m\ddot{y} + F_{m,y_1} + F_{m,y_2} + F_{c,y} = -mg + F_{\varepsilon_y} \\ &m\ddot{z} + F_{m,z_1} + F_{m,z_2} = R_z \\ &I_d\ddot{\theta}_x + I_p\Omega\dot{\theta}_y + \left(T_{m,x_1} + T_{m,x_2}\right) + \left(F_{m,y_1} - F_{m,y_2}\right) d + F_{c,y}\frac{l}{2} = T_{\gamma_x} \\ &I_d\ddot{\theta}_y - I_p\Omega\dot{\theta}_x + \left(T_{m,y_1} + T_{m,y_2}\right) - \left(F_{m,x_1} - F_{m,x_2}\right) d - F_{c,x}\frac{l}{2} = T_{\gamma_y} \\ &I_p\ddot{\theta}_z + c_\Omega\dot{\theta}_z = 0 \end{aligned} \tag{B.1}$$

Constant stiffness coefficients are calculated as derivatives of forces and torques evaluated at the equilibrium position to develop a linearised model of the dynamic behaviour of the rotor, starting from Eq. (6).

$$\begin{aligned} F_{m_{linear}}(x,y) &= F_m\left(x_{eq}, y_{eq}\right) + \left.\frac{\partial F_m}{\partial \bar{x}_z}\right|_{x=x_{eq},y=y_{eq}} \bar{x}_z + \left.\frac{\partial F_m}{\partial \bar{y}_z}\right|_{x=x_{eq},y=y_{eq}} \bar{y}_z \\ T_{m_{linear}}(x,y) &= T_m\left(x_{eq}, y_{eq}\right) + \left.\frac{\partial T_m}{\partial \bar{x}_z}\right|_{x=x_{eq},y=y_{eq}} \bar{x}_z + \left.\frac{\partial T_m}{\partial \bar{y}_z}\right|_{x=x_{eq},y=y_{eq}} \bar{y}_z \end{aligned} \tag{B.2}$$

The approximated magnetic analytical formulations of Eq. (6) are used to numerically evaluate the force and torque derivatives. After substituting Eq. (B.2) in Eq. (B.1), the system becomes:

$$\begin{aligned} &m\ddot{x} \\ &+ \left.\frac{\partial F_{m,x_1}}{\partial x}\right|_{eq} x - \left.\frac{\partial F_{m,x_1}}{\partial x}\right|_{eq} d\theta_y + \left.\frac{\partial F_{m,x_2}}{\partial x}\right|_{eq} x + \left.\frac{\partial F_{m,x_2}}{\partial x}\right|_{eq} d\theta_y \\ &+ \left.\frac{\partial F_{m,x_1}}{\partial y}\right|_{eq} \bar{y} + \left.\frac{\partial F_{m,x_1}}{\partial y}\right|_{eq} d\theta_x + \left.\frac{\partial F_{m,x_2}}{\partial y}\right|_{eq} \bar{y} - \left.\frac{\partial F_{m,x_2}}{\partial y}\right|_{eq} d\theta_x \\ &+ C_{c,x}\dot{x} - C_{c,x}\frac{l}{2}\dot{\theta}_y = F_{\varepsilon_x} \end{aligned} \tag{B.3}$$

$$\begin{aligned} &m\ddot{y} \\ &+ \left.\frac{\partial F_{m,y_1}}{\partial x}\right|_{eq} x - \left.\frac{\partial F_{m,y_1}}{\partial x}\right|_{eq} d\theta_y + \left.\frac{\partial F_{m,y_2}}{\partial x}\right|_{eq} x + \left.\frac{\partial F_{m,y_2}}{\partial x}\right|_{eq} d\theta_y \\ &+ \left.\frac{\partial F_{m,y_1}}{\partial y}\right|_{eq} \bar{y} + \left.\frac{\partial F_{m,y_1}}{\partial y}\right|_{eq} d\theta_x + \left.\frac{\partial F_{m,y_2}}{\partial y}\right|_{eq} \bar{y} - \left.\frac{\partial F_{m,y_2}}{\partial y}\right|_{eq} d\theta_x \\ &+ C_{c,y}\dot{y} + C_{c,y}\frac{l}{2}\dot{\theta}_x = F_{\varepsilon_y} \end{aligned} \tag{B.4}$$

Table B.5
Model updating parameters.

Model updating parameter	Value
k_x	0.5822
k_y	1.8462

Table B.6
Translational DOF stiffness value.

Stiffness parameter	Value
$K_{F_{xx}}$	45.3488 N/m
$K_{F_{yy}}$	37.5950 N/m

$$m\ddot{z} + \left.\frac{\partial F_{m,z}}{\partial z}\right|_{eq} z = R_z \tag{B.5}$$

$$\begin{aligned} &I_d\ddot{\theta}_x + I_p\Omega\dot{\theta}_y \\ &+ \left(\left.\frac{\partial T_{m,x_1}}{\partial x}\right|_{eq} + \left.\frac{\partial F_{m,y_1}}{\partial x}\right|_{eq} d\right)\left(x - d\theta_y\right) \\ &+ \left(\left.\frac{\partial T_{m,x_1}}{\partial y}\right|_{eq} + \left.\frac{\partial F_{m,y_1}}{\partial y}\right|_{eq} d\right)\left(\bar{y} + d\theta_x\right) \\ &+ \left(\left.\frac{\partial T_{m,x_2}}{\partial x}\right|_{eq} - \left.\frac{\partial F_{m,y_2}}{\partial x}\right|_{eq} d\right)\left(x + d\theta_y\right) \\ &+ \left(\left.\frac{\partial T_{m,x_2}}{\partial y}\right|_{eq} - \left.\frac{\partial F_{m,y_2}}{\partial y}\right|_{eq} d\right)\left(\bar{y} - d\theta_x\right) \\ &+ \left(C_{c,y}\dot{y} + C_{c,y}\frac{l}{2}\dot{\theta}_x\right)\frac{l}{2} = T_{\gamma_x} \end{aligned} \tag{B.6}$$

$$\begin{aligned} &I_d\ddot{\theta}_y - I_p\Omega\dot{\theta}_x \\ &+ \left(\left.\frac{\partial T_{m,y_1}}{\partial x}\right|_{eq} - \left.\frac{\partial F_{m,x_1}}{\partial x}\right|_{eq} d\right)\left(x - d\theta_y\right) \\ &+ \left(\left.\frac{\partial T_{m,y_1}}{\partial y}\right|_{eq} - \left.\frac{\partial F_{m,x_1}}{\partial y}\right|_{eq} d\right)\left(\bar{y} + d\theta_x\right) \\ &+ \left(\left.\frac{\partial T_{m,y_2}}{\partial x}\right|_{eq} + \left.\frac{\partial F_{m,x_2}}{\partial x}\right|_{eq} d\right)\left(x + d\theta_y\right) \\ &+ \left(\left.\frac{\partial T_{m,y_2}}{\partial y}\right|_{eq} + \left.\frac{\partial F_{m,x_2}}{\partial y}\right|_{eq} d\right)\left(\bar{y} - d\theta_x\right) \\ &- \left(C_{c,x}\dot{x} - C_{c,x}\frac{l}{2}\dot{\theta}_y\right)\frac{l}{2} = T_{\gamma_y} \end{aligned} \tag{B.7}$$

$$I_p\ddot{\theta}_z + C_\Omega\dot{\theta}_z = 0 \tag{B.8}$$

Approximations are done during the calculation of magnetic maps, so these stiffness values need to be tuned to obtain the right values. The applied procedure consists of respectively multiplying the generalised magnetic force derivates by tuning parameters k_x and k_y, and then comparing the tuned resulting natural frequencies with the ones of an experimental frequency analysis, as the one shown in Fig. 4, until the values match each other. Table B.5 shows the model updating parameters used for this application.

Hence, the stiffness values related to forces calculated for the linear model are listed in Table B.6,

Values from Table B.6 are to be divided by 2 to obtain the stiffness of the single springs that model the magnetic supports.

References

[1] V. Cirimele, L. Dimauro, M. Repetto, E. Bonisoli, Multi-objective optimisation of a magnetic gear for powertrain applications, Int. J. Appl. Electromagn. Mech. 60 (S1) (2019) S25 – S34, http://dx.doi.org/10.3233/JAE-191103.

[2] L. Dimauro, E. Bonisoli, M. Repetto, Dynamic behaviour and magneto-mechanical efficiency of a contactless magnetic transmission, Conference Proceedings of the Society for Experimental Mechanics Series (2023) 129–138, http://dx.doi.org/10.1007/978-3-031-04098-6_14.

[3] G. Schweitzer, Applications and research topics for active magnetic bearings, in: K. Gupta (Ed.), IUTAM Symposium on Emerging Trends in Rotor Dynamics, Springer Netherlands, Dordrecht, 2011, pp. 263–273, http://dx.doi.org/10.1007/978-94-007-0020-8_23.

[4] J.-P. Yonnet, G. Lemarquand, S. Hemmerlin, E. Olivier-Rulliere, Stacked structures of passive magnetic bearings, J. Appl. Phys. 70 (10) (1991) 6633–6635, http://dx.doi.org/10.1063/1.349857.

[5] H. Bangcheng, Z. Shiqiang, W. Xi, Y. Qian, Integral design and analysis of passive magnetic bearing and active radial magnetic bearing for agile satellite application, IEEE Trans. Magn. 48 (6) (2012) 1959–1966, http://dx.doi.org/10.1109/TMAG.2011.2180731.

[6] J. Fang, Y. Le, J. Sun, K. Wang, Analysis and design of passive magnetic bearing and damping system for high-speed compressor, IEEE Trans. Magn. 48 (9) (2012) 2528–2537, http://dx.doi.org/10.1109/TMAG.2012.2196443.

[7] A. Filatov, E. Maslen, Passive magnetic bearing for flywheel energy storage systems, IEEE Trans. Magn. 37 (6) (2001) 3913–3924, http://dx.doi.org/10.1109/20.966127.

[8] L. Piancastelli, N. Daidzic, L. Frizziero, I. Rocchi, Analysis of automotive diesel conversions with KERS for future aerospace applications, Int. J. Heat Technol. 31 (1) (2013) 143–153, http://dx.doi.org/10.18280/ijht.310119.

[9] L. Pugi, M. Pagliai, A. Nocentini, G. Lutzemberger, A. Pretto, Design of a hydraulic servo-actuation fed by a regenerative braking system, Appl. Energy 187 (2017) 96–115, http://dx.doi.org/10.1016/j.apenergy.2016.11.047.

[10] F. Bottiglione, G. Mantriota, Effect of the ratio spread of CVU in automotive kinetic energy recovery systems, J. Mech. Des. 135 (6) (2013) 061001, http://dx.doi.org/10.1115/1.4024121.

[11] N.F. Ershad, R.T. Mehrjardi, M. Ehsani, Development of a kinetic energy recovery system using an active electromagnetic slip coupling, IEEE Trans. Transp. Electrif. 5 (2) (2019) 456–464, http://dx.doi.org/10.1109/TTE.2019.2891045.

[12] M.V. Terzic, D.S. Mihic, S.N. Vukosavić, Design of high-speed, low-inertia induction machines with drag-cup rotor, IEEE Trans. Energy Convers. 29 (1) (2014) 169–177, http://dx.doi.org/10.1109/TEC.2013.2289352.

[13] J. Ji, Dynamics of a jeffcott rotor-magnetic bearing system with time delays, Int. J. Non-Linear Mech. 38 (9) (2003) 1387–1401, http://dx.doi.org/10.1016/S0020-7462(02)00078-1.

[14] A. Dolev, S. Tresser, I. Bucher, Balancing high-speed rotors at low speed using optimized parametric excitation and tuned nonlinear feedback, Int. J. Non-Linear Mech. 139 (2022) 103873, http://dx.doi.org/10.1016/j.ijnonlinmec.2021.103873.

[15] H. Yao, Y. Wang, Y. Cao, B. Wen, Multi-stable nonlinear energy sink for rotor system, Int. J. Non-Linear Mech. 118 (2020) http://dx.doi.org/10.1016/j.ijnonlinmec.2019.103273.

[16] E. Bonisoli, C. Delprete, Nonlinear and linearised behaviour of the levitron®, Meccanica 51 (4) (2016) 763–784, http://dx.doi.org/10.1007/s11012-015-0238-5.

[17] G. Genta, Dynamics of Rotating Systems, Mechanical Engineering Series, Springer New York, 2007.

[18] S. Earnshaw, On the nature of the molecular forces which regulate the constitution of the luminiferous ether, Trans. Camb. Philos. Soc. 7 (1848) 97.

[19] L. Romero, Spin stabilized magnetic levitation of horizontal rotors, SIAM J. Appl. Math. 63 (6) (2003) 2176–2194, http://dx.doi.org/10.1137/S0036139902406899.

[20] E. Bonisoli, L. Dimauro, S. Venturini, S.P. Cavallaro, Experimental detection of nonlinear dynamics using a laser profilometer, Appl. Sci. 13 (5) (2023) 3295, http://dx.doi.org/10.3390/app13053295.

[21] E. Bonisoli, S. Venturini, S.P. Cavallaro, Nonlinear characterisation of a rotor on passive magnetic supports, Int. J. Mech. Control 23 (1) (2022) 121–128.

[22] A. D'Angola, G. Carbone, L. Mangialardi, C. Serio, Non-linear oscillations in a passive magnetic suspension, Int. J. Non-Linear Mech. 41 (9) (2006) 1039–1049, http://dx.doi.org/10.1016/j.ijnonlinmec.2006.10.013.

[23] J. Ji, A. Leung, Non-linear oscillations of a rotor-magnetic bearing system under superharmonic resonance conditions, Int. J. Non-Linear Mech. 38 (6) (2003) 829–835, http://dx.doi.org/10.1016/S0020-7462(01)00136-6.

[24] C. Bai, H. Zhang, Q. Xu, Subharmonic resonance of a symmetric ball bearing-rotor system, Int. J. Non-Linear Mech. 50 (2013) 1–10, http://dx.doi.org/10.1016/j.ijnonlinmec.2012.11.002.

[25] F. Ehrich, High order subharmonic response of high speed rotors in bearing clearance, Trans. ASME 110 (1) (1988) 9–16, http://dx.doi.org/10.1115/1.3269488.

[26] L. Hou, Y. Chen, Analysis of 1/2 sub-harmonic resonance in a maneuvering rotor system, Sci. China Technol. Sci. 57 (1) (2014) 203–209, http://dx.doi.org/10.1007/s11431-013-5418-8.

[27] N. Yoshida, T. Takano, H. Yabuno, T. Inoue, Y. Ishida, 1/2-Order subharmonic resonances in horizontally supported jeffcott rotor, Proc. ASME Des. Eng. Tech. Conf. 1 (PARTS A AND B) (2011) 893–902, http://dx.doi.org/10.1115/DETC2011-47605.

[28] E. Bonisoli, L. Dimauro, S. Venturini, LUPOS: Open-source scientific computing in structural dynamics, Conference Proceedings of the Society for Experimental Mechanics Series (2023) 177–188, http://dx.doi.org/10.1007/978-3-031-34946-1_23.

[29] H. Nagaraj, Investigation of magnetic fields and forces arising in open-circuit-type magnetic bearings, Tribol. Trans. 31 (2) (1988) 192–201, http://dx.doi.org/10.1080/10402008808981815.

[30] E. Bonisoli, A. Vigliani, Identification techniques applied to a passive elasto-magnetic suspension, Mech. Syst. Signal Process. 21 (3) (2007) 1479–1488, http://dx.doi.org/10.1016/j.ymssp.2006.05.009.

[31] E. Bonisoli, A. Vigliani, Passive elasto-magnetic suspensions: nonlinear models and experimental outcomes, Mech. Res. Commun. 34 (4) (2007) 385–394, http://dx.doi.org/10.1016/j.mechrescom.2007.02.005.

[32] A.O. Oyelade, Experiment study on nonlinear oscillator containing magnetic spring with negative stiffness, Int. J. Non-Linear Mech. 120 (2020) http://dx.doi.org/10.1016/j.ijnonlinmec.2019.103396.

[33] W. Robertson, B. Cazzolato, A. Zander, Theoretical analysis of a non-contact spring with inclined permanent magnets for load-independent resonance frequency, J. Sound Vib. 331 (6) (2012) 1331–1341, http://dx.doi.org/10.1016/j.jsv.2011.11.011.

[34] G. Iuso, G. Virone, G. Cafiero, E. Bonisoli, D. Lisitano, S. Venturini, Aeroelastic-structural coupling in antenna prototype for windy open-space, 8th International Conference on Computational Methods for Coupled Problems in Science and Engineering, COUPLED PROBLEMS 2019, (2021) 481–492.

[35] A. Masoumi, M. Barbieri, F. Pellicano, A. Zippo, M. Strozzi, Dynamic imbalance of high-speed planetary gears, Int. J. Cond. Monit. 7 (1) (2017) 2–6, http://dx.doi.org/10.1784/204764217820441008.

[36] E. Pennestri, V. Rossi, P. Salvini, P.P. Valentini, Review and comparison of dry friction force models, Nonlinear Dynam. 83 (2016) 1785–1801, http://dx.doi.org/10.1007/s11071-015-2485-3.

[37] A. Vardhan, Vibrations of a non jeffcott rotor with one non linear bearing, Appl. Mech. Mater. 232 (2012) 450–455, http://dx.doi.org/10.4028/www.scientific.net/AMM.232.450.

[38] T.d.P. Sales, E. Spuldaro, L.F. Damy, D.A. Rade, Dynamic modeling of flexible rotors mounted on an elastic base undergoing arbitrary attitude motion, Mech. Mach. Sci. 61 (2019) 562–576, http://dx.doi.org/10.1007/978-3-319-99268-6_39.

[39] A. Kyprianou, J.E. Mottershead, Uncertain systems: Modelling and updating, 18th International Congress on Sound and Vibration 2011, ICSV 2011 2 (2011) 995–1002.

[40] D. Bernal, M.D. Ulriksen, E. Memarzadeh, Static constraints in direct model updating, Mech. Syst. Signal Process. 163 (2022) 108170, http://dx.doi.org/10.1016/j.ymssp.2021.108170.